Research Article

Cancer Immunology Research

Rational Selection of Syngeneic Preclinical Tumor Models for Immunotherapeutic Drug Discovery

Suzanne I.S. Mosely[1], John E. Prime[1], Richard C.A. Sainson[1], Jens-Oliver Koopmann[1], Dennis Y.Q. Wang[2], Danielle M. Greenawalt[3], Miika J. Ahdesmaki[2], Rebecca Leyland[1], Stefanie Mullins[1], Luciano Pacelli[1], Danielle Marcus[1], Judith Anderton[1], Amanda Watkins[1], Jane Coates Ulrichsen[1], Philip Brohawn[4], Brandon W. Higgs[4], Matthew McCourt[1], Hazel Jones[1], James A. Harper[1], Michelle Morrow[1], Viia Valge-Archer[1], Ross Stewart[1], Simon J. Dovedi[1], and Robert W. Wilkinson[1]

Abstract

Murine syngeneic tumor models are critical to novel immuno-based therapy development, but the molecular and immunologic features of these models are still not clearly defined. The translational relevance of differences between the models is not fully understood, impeding appropriate preclinical model selection for target validation, and ultimately hindering drug development. Across a panel of commonly used murine syngeneic tumor models, we showed variable responsiveness to immunotherapies. We used array comparative genomic hybridization, whole-exome sequencing, exon microarray analysis, and flow cytometry to extensively characterize these models, which revealed striking differences that may underlie these contrasting response profiles. We identified strong differential gene expression in immune-related pathways and changes in immune cell–specific genes that suggested differences in tumor immune infiltrates between models. Further investigation using flow cytometry showed differences in both the composition and magnitude of the tumor immune infiltrates, identifying models that harbor "inflamed" and "non-inflamed" tumor immune infiltrate phenotypes. We also found that immunosuppressive cell types predominated in syngeneic mouse tumor models that did not respond to immune-checkpoint blockade, whereas cytotoxic effector immune cells were enriched in responsive models. A cytotoxic cell–rich tumor immune infiltrate has been correlated with increased efficacy of immunotherapies in the clinic, and these differences could underlie the varying response profiles to immunotherapy between the syngeneic models. This characterization highlighted the importance of extensive profiling and will enable investigators to select appropriate models to interrogate the activity of immunotherapies as well as combinations with targeted therapies *in vivo*. *Cancer Immunol Res; 5(1); 29–41. ©2016 AACR.*

Introduction

Recent clinical successes treating tumors with immunotherapies, including approval of the immune-checkpoint blockade antibodies ipilimumab (anti–CTLA-4) and nivolumab and pembrolizumab (anti–PD-1), demonstrate the potential to transform treatment paradigms and improve patient outcomes (1–3). These treatments represent a shift in the approach to cancer therapy as they do not target the tumor cells but instead target the immune system to circumvent inhibitory pathways that attenuate effective antitumor immune responses. Despite these successes, responses to immunotherapy usually remain restricted to a subpopulation of patients (4, 5). In order to broaden the cancer patient population benefiting from immunotherapy, a greater understanding is needed of the factors that affect response and the potential for combination of different therapies. It is clear that T-cell infiltration varies greatly between individual tumors, patients, and disease types, with some considered to harbor more immunogenic (e.g., "hot"/"inflamed") tumors (6, 7), characterized by greater T-cell infiltration and Th1 cytokine expression, and overlapping drivers of immunosuppression. In contrast, other tumors may be characterized by a sparse T-cell infiltrate (e.g., immunologically "cold"), potentially as a consequence of reduced immunogenicity. The phenotype of the tumor immune infiltrate correlates with both patient prognosis (8) and outcome following immunotherapy (9). Intrinsic tumor characteristics such as neoantigen load can also affect response to immunotherapy (10, 11), possibly by modulating tumor immunogenicity (12).

Human xenograft tumor models, in which human tumor cell lines are implanted in mice, have played a critical role in understanding traditional cytotoxic or targeted cancer therapies. However, in the context of immunotherapy, these routinely used and well-characterized models are not suitable, because they lack an

[1]MedImmune Ltd, Cambridge, United Kingdom. [2]AstraZeneca Ltd, Cambridge, United Kingdom. [3]AstraZeneca Ltd, Waltham, Massachusetts. [4]MedImmune LLC, Gaithersburg, Maryland.

Note: Supplementary data for this article are available at Cancer Immunology Research Online (http://cancerimmunolres.aacrjournals.org/).

S.I.S. Mosely, J.E. Prime, and R.C.A. Sainson contributed equally to this article.

Current address for R.C.A. Sainson: Kymab Ltd, Cambridge, United Kingdom; current address for D.Y.Q. Wang, University of Sheffield, Sheffield, United Kingdom; current address for L. Pacelli, Chiesi Farmaceutici S.p.A., Parma, Italy; and current address for H. Jones and V. Valge-Archer, AstraZeneca Ltd, Cambridge, United Kingdom.

Corresponding Author: Suzanne I.S. Mosely, MedImmune Ltd, Aaron Klug Building, Granta Park, Cambridge CB21 6GH, United Kingdom. Phone: 02037496425; Fax: 012-2347-1472; E-mail: moselys@medimmune.com

doi: 10.1158/2326-6066.CIR-16-0114

intact immune system. Several immunocompetent mouse model systems can be used to study immunotherapies, but each brings with it a series of challenges and limitations (reviewed in refs. 13 and14). For example, genetically engineered mouse models (GEMM) recapitulate the anatomical location and encompass some disease-specific mutations frequently observed in human cancer, but they require large colonies of mice, have extended latency periods and, in contrast to the clinical setting, often display limited mutational burden and minimal genetic mosaicism (15). Alternatively, models based on subcutaneous or orthotopic implantation of syngeneic tumor cell lines have short latency periods, are reproducible, and high-throughput; on the basis of this, they have been the workhorse of cancer immunology for several decades (13). These tumor models have been invaluable in providing preclinical proof of concept for candidate immunotherapeutic drugs (16, 17), as well as building an understanding of mechanism of action and evaluating potential biomarkers of response (18, 19). However, to date, the majority of studies have been performed in a small number of models (compared with xenografts, ref. 14) and, despite their widespread use, surprisingly little is known about the genotypes and phenotypes of these syngeneic murine tumor models (14). Ultimately, a better understanding of these models is required to enable appropriate model selection and to permit both data interpretation and extrapolation to the clinic (13, 14).

Here, we describe a comprehensive characterization of the genomic, transcriptomic, and immunologic composition of several murine syngeneic tumor models. Using flow cytometry, we characterized the tumor immune infiltrate, the spleen and tumor-draining lymph nodes (TDLN) in a panel of our most frequently used models. This enabled us to examine whether the genotype and gene expression profile of the tumor cells associated with their immunophenotype *in vivo* and determine how this related to response following immune-checkpoint blockade. This study highlights the need for extensive characterization of models used for preclinical immunotherapy research, and provides data that will, based on the proposed mechanism of action of the therapy being evaluated, support investigators in selecting appropriate models using hypothesis-driven rationales. It also forms the basis of a dataset that will increase the translational relevance of studies, by allowing parallels to be drawn between models and human disease phenotypes. Moreover, these data can be readily applied to expedite the discovery and development of novel immunotherapies by increasing the efficiency of preclinical drug development.

Materials and Methods

Tumor models

An overview of the experiments performed is shown in Supplementary Fig. S1. All *in vivo* experiments were performed in accordance with the UK Animal (Scientific Procedures) Act 1986 and the EU Directive 86/609, under a UK Home Office Project License and approved by the Babraham Institute Animal Welfare and Ethical Review Body, using guidelines outlined by Workman and colleagues (20). C57BL/6 and BALB/c mice were supplied by Charles River UK at 8 to 10 weeks of age and >18g and housed under specific pathogen-free conditions in Tecniplast Green Line IVC Sealsafe cages holding a maximum of 6 animals with irradiated aspen chip bedding, Nestlets nesting material, a cardboard tunnel and wooden chew blocks. Mice were housed on a 12/12 light/dark cycle, with *ad libitum* UV-treated water and RM1 rodent diet.

Cells (100 μL) in PBS were subcutaneously injected into the right flanks of mice (unless otherwise stated; details of the cell lines and cell numbers are given in Supplementary Table S1). Cells did not undergo any *in vivo* passaging (except for the B16F10 AP-3 cell line) and were maintained under limited passage from original stocks (typically under 5). We did not undertake additional independent validation. Tumor volume was measured using the formula $(\text{width}^2 \times \text{length})/2$, and tumors were collected when reaching an average of 150 mm^3. For the Pan02 cell line, 50 μL of cells in ice-cold matrigel (Corning) were surgically implanted into the pancreas tail. For tumor growth studies, mice were injected intraperitoneally with 10 mg/kg of either anti–CTLA-4 (mouse IgG2b, clone 9D9; Biolegend) or anti–PD-L1 (rat IgG2b, clone 10F.9G2; BioXCell) or the respective isotype controls (αNIP; MedImmune).

Array comparative genomic hybridization (aCGH)

Microarray services were provided by Almac Diagnostics. Genomic DNA was extracted from one sample of each mouse tumor cell line using the DNeasy Blood and Tissue Kit (Qiagen) and quality controlled (OD A260/230 ratio $\geq$ 1.8) using a 2100 Bioanalyzer (Agilent). Samples were 2-color labeled using the genomic DNA labeling kit PLUS (Agilent), hybridized on Agilent Mouse genome CGH 1 × 224K oligo microarrays using the Oligo aCGH Hybridization kit (Agilent) and scanned on an Agilent Microarray scanner. Reference mouse genomic DNA (Merck) was used as a control. All microarray data are deposited into GEO (accession number GSE85509). After normalization to the control mouse genome, probe $\log_2$ ratios for autosomal genes were converted to copy-number variation (CNV) values (Supplementary Table S2 and Supplementary Dataset).

Whole-exome sequencing (WES)

DNA was extracted from cell lines using the DNeasy Blood and Tissue kit (Qiagen). DNA samples were evaluated using an E-Gel (Invitrogen) and PicoGreen fluorometry to measure quality and quantity, respectively. DNA samples were then physically sheared to the desired size using a Covaris E220 Focused-ultrasonicator. Library preparation and enrichment were carried out using an Agilent SureSelectXT Mouse All Exon 49.6Mb design, followed by sequencing on an Illumina HiSeq 2000. Basecall files (*.bcl) were de-multiplexed and converted to fastq.gz format using CASAVA v1.8.2 (Illumina). CrossMap (21) was used to lift the BED files over to mm10 reference for variant calling. The reads were aligned using BWA (22) and variants were called using FreeBayes (23) and VarDict (24). Copy number was inferred from the exome data using Seq2C and CNVKit (25) for approximately 1500 immune system and oncology-related genes. Variants were strain-specifically annotated using data downloaded from ftp://ftp-mouse.sanger.ac.uk/REL-1505-SNPs_Indels/strain_specific_vcfs/ for C57BL_6NJ, BALB_cJ, and DBA_1J. Sequencing data were deposited in the European Nucleotide Archive (accession PRJEB12925).

Targeted sequencing

DNA was isolated from fresh-frozen tumor tissue utilizing the Qiagen MagAttract kit and concentrations determined by Nanodrop spectrophotometry. Focused amplicon sequencing

of 64 genes commonly mutated in cancer patients (based on proprietary datasets and the COSMIC database; ref. 26) was carried out utilizing a custom AmpliSeq panel (Life Technologies) to confirm their mutation status. Two pools of amplicons were generated and 20 ng of DNA was utilized for each pool. The manufacturer's protocol was followed for target amplification, adapter ligation, and purification. Libraries were sequenced on an Ion PGM instrument utilizing the 318 chip. Reads were aligned with Bowtie v2.0 (27) using the mouse reference version mm10 (B6 strain). Single nucleotide variants were called using VarScan v2.3.2 (28) with minimum average quality = 30, minimum variant allele read count = 5, and Fisher exact *t* test $P < 0.01$. Minimum variant allele frequencies of 7% were called with a minimum of 200× total depth at the locus. Annotation was conducted using Annovar (29).

Transcriptomics

Microarray services were provided by Almac Diagnostics. RNA was extracted from the tumor, spleen, and lymph node (LN) tissues from each model using RNAStat 60 (Amsbio), and quality of total RNA was determined using a 2100 Bioanalyzer (Agilent). After amplification using the WT-Ovation Pico amplification kit (NuGEN Technologies), cDNA was generated using WT-Ovation Exon module. After quality testing, cDNA was fragmented, labeled and hybridized using the FL-Ovation cDNA Biotin Module V2 (NuGEN Technologies) to Mouse Exon 1.0 ST arrays (Affymetrix). All microarray data are deposited into GEO (accession number GSE85509). Microarray data underwent Robust Multichip Algorithm preprocessing and normalization in Omicsoft ArrayStudio. Exon probes (1,192,934) remained with a probe detection $P \leq 0.05$. Quality control excluded two outliers. Log_2 transcript expression values were determined as the median of detected core probes.

To enable cross-comparison of tumor samples between models, five simulated pooled samples (SPS) were generated by proportional resampling with replacement of the log_2 expression intensities for each gene (R and Omicsoft ArrayStudio). The SPS tumor control group was compared with tumor samples from each model to identify differentially expressed genes (DEG) using empirical Bayesian analysis [including vertical (within a given comparison) *P* value adjustment for multiple testing; Fios Genomics]. LN and spleen samples were compared with their tissue, strain, and sex-matched controls. DEGs were selected using both FDR adjusted *P* value ≤ 0.05 (Benjamini and Hochberg method) and fold change ≥ 2.0 or ≤ -2.0.

DEGs underwent functional enrichment and network analyses using Ingenuity Pathway Analysis (IPA, Ingenuity Systems). Enrichment analysis results were cross-compared using the IPA comparison tool. The differentially regulated non-disease canonical pathways with the top ten highest and lowest activation Z scores per model were ranked by summed absolute Z score for all 15 models and plotted in a heatmap. Normalized log_2 gene expression intensity per tumor sample for 96 cell type–annotated genes from the Nanostring nCounter PanCancer Immune Profiling Panel gene-list underwent hierarchical cluster analysis (HCA; normalized, linkage = Ward and distance = Euclidean) to cluster samples only, with genes ordered by immune cell type annotation (Matlab).

Flow cytometry

Tumors were disaggregated using the GentleMACS Mouse Tumor Dissociation kit (Miltenyi Biotech). Spleens and TDLNs were dissociated through a 70-μm nylon cell strainer. Spleens were resuspended in red blood cell lysis buffer (Sigma) for 1 minute. All cells were then stained with a viability dye (Thermo Fisher) and blocked with antibodies to CD16/CD32 (eBioscience) before staining with fluorescence-conjugated antibodies (Supplementary Table S4) in flow cytometry staining buffer with Brilliant Stain Buffer (BD Biosciences). Intracellular staining was performed using the FoxP3/transcription factor staining buffer set (eBioscience) and cells were fixed in 3.7% formaldehyde/PBS. Counting beads (123Count eBeads; eBioscience) were added to the samples before acquisition on an LSRFortessa (BD Biosciences) and analysis using FlowJo (TreeStar). Gating strategies are shown in Supplementary Fig. S2. To enable comparisons between tumors, cell counts were normalized by dividing the cell count obtained using the counting beads by the tumor volume.

Cytokine quantification

Tumors were snap-frozen in liquid nitrogen, then lysed on a TissueLyser II (Qiagen) in 1% Triton-X/PBS with phosphatase inhibitors (PhosSTOP; Roche), protease inhibitors (cOmplete; Roche), and tungsten carbide beads (Qiagen). Lysates were freeze-thawed, centrifuged and diluted to 0.5 mg/mL before analysis of 10 cytokines using the mouse Proinflammatory Panel 1 V-PLEX immunoassay (Meso Scale Discovery). Data were log transformed and plotted using Matlab.

Statistical analyses

Flow cytometry data were analyzed in GraphPad Prism using one-way ANOVA with Tukey correction for multiple comparisons. For tumor growth studies, group sizes were determined using power analyses based on the variability of the models in pilot studies. Tumor growth data were log_{10} transformed, and the effectiveness of the therapy (Tr) with respect to the baseline treatment performance was assessed with a linear mixed-effect model (30, 31). The Yij, representing log_{10}-transformed *i*th tumor volume observed at *j*th assessment point (T), follows the linear growth model: $Yij = a0i + a1i * Tj + eij$, where a0i and a1i denote individual intercept and slope parameters, respectively, and $eij \sim N(0,\sigma)$ represents model error. Both intercept and slope are assumed to express random effects:

$a0i = g00 + g01*Tri + u0i$, $a1i = g10 + g11*Tri + u1i$, with $u0i \sim N(0, \sigma0)$ and $u1i \sim N(0, \sigma1)$. The parameters g00, g10, and g01, g11 represent the parameter's fixed effects; σ, and σ0, σ1 correspond to intra- and intertumor variance, respectively. Models were defined as "responsive" if the growth kinetics of the treated group compared with the control group was significantly different ($P < 0.05$).

Results

Model-dependent differences in antitumor response to anti–CTLA-4 and anti–PD-L1

During our preclinical investigation of CTLA-4 and PD-L1 as targets for immune-checkpoint blockade, we tested the antitumor activity of surrogate antibodies in several murine syngeneic tumor models (32). Significant tumor growth inhibition was seen following anti–CTLA-4 treatment in the CT26 ($P \leq$

0.0001) and RENCA ($P \leq 0.0001$) models (Fig. 1A), whereas PD-L1 demonstrated activity only in the CT26 model ($P \leq 0.0001$; Fig. 1B). This highlighted a need to better understand the underlying immunobiology of murine syngeneic tumor models in order to identify potential drivers of response and enable rational selection of appropriate models for preclinical activity testing.

Genomic analysis reveals a high degree of diversity in copy number variations

We performed genome-wide aCGH analysis on 16 *in vitro* murine tumor cell lines to gain an understanding of broad amplification and deletion events. CNV levels were not affected by the method of tumor cell line generation because CNV frequency of carcinogen-induced CT26, genetically induced

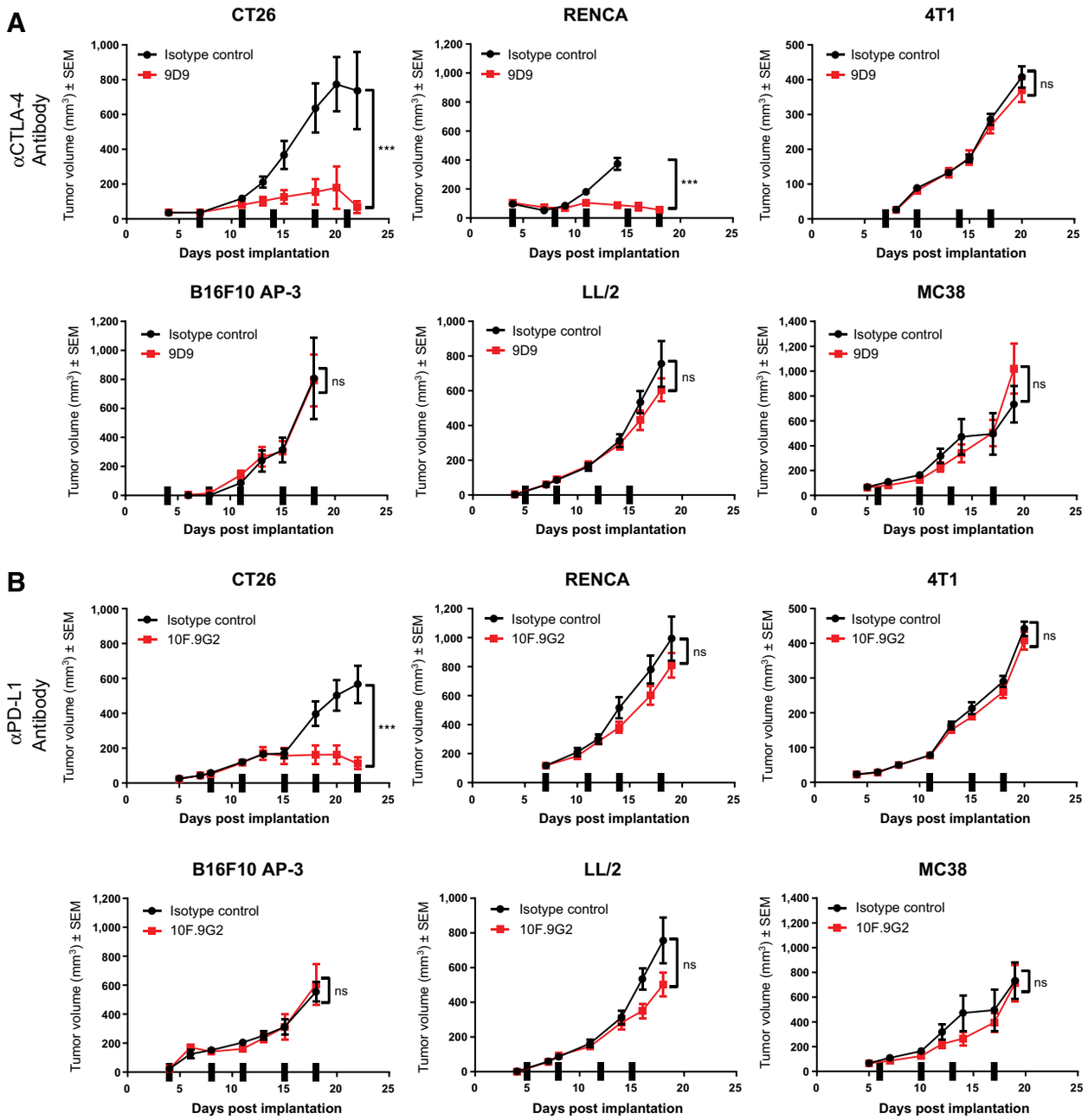

Figure 1.

The antitumor activity of anti–CTLA-4 and anti–PD-L1 treatment varies across a range of syngeneic models. Tumor growth curves for 6 subcutaneous murine syngeneic tumor models treated with either (**A**) CTLA-4 antibody clone 9D9 (10 mg/kg) or (**B**) PD-L1 antibody clone 10F.9G2 (10 mg/kg). Treatment was given by intraperitoneal injection on the days marked with ticks on the *x*-axis of the graphs. $n \geq 6$ mice per group. ***, $P < 0.0001$, ns: nonsignificant $P \geq 0.05$, linear mixed-effect model test. Data are representative of at least two independent experiments.

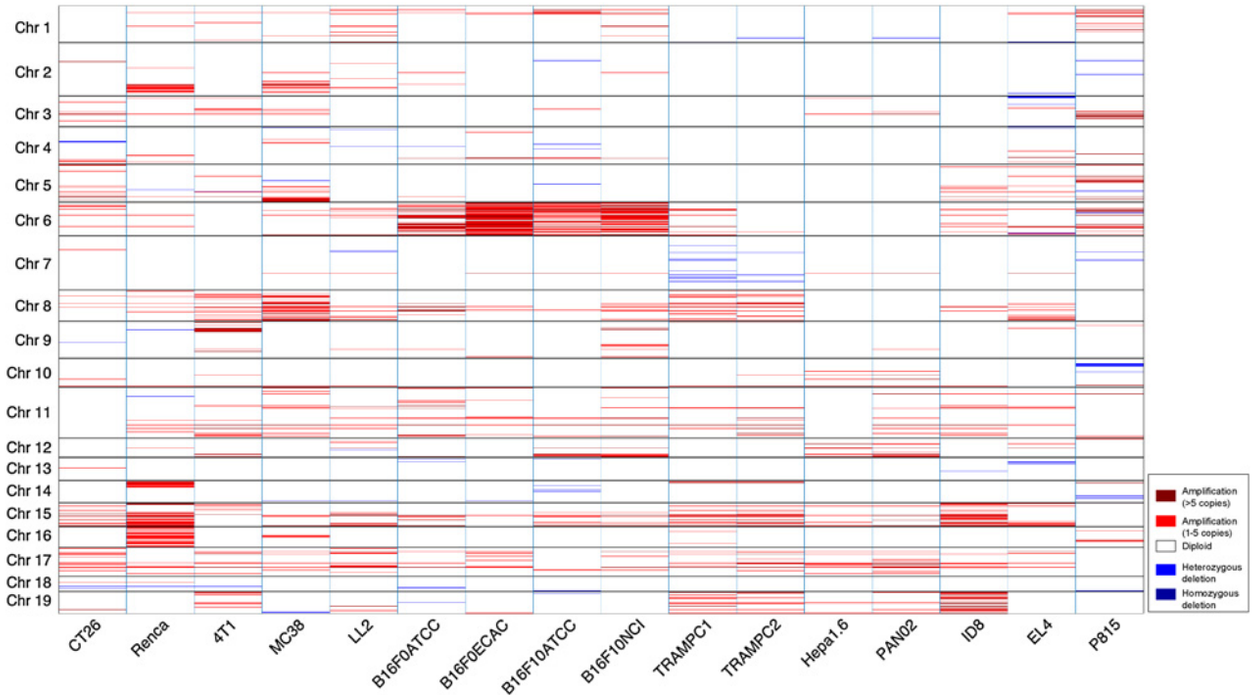

Figure 2.

CNVs strongly differ between the cell lines. CNVs for 16 cell lines determined using aCGH analysis. Genomic regions are sorted by chromosome, and copy number changes of roughly 10 genes displayed, with amplifications $\leq$ 5 copies as light red lines, amplifications > 5 copies as dark red lines, loss of one copy as light blue lines, and deletions of both copies as dark blue lines.

TRAMP-C2, and spontaneous LL/2 cell lines were not markedly dissimilar (5.74%, 5.75%, and 5.04% respectively; Fig. 2). No difference in the overall burden of genomic aberrations was seen in the CT26 cell line compared with the others (5.74% of genes studied had CNV in CT26 vs. a mean of 6.05% across the other 15 cell lines). In order to assess CNVs against a paired background strain as opposed to a reference genome, we also investigated somatic gene copy number using WES (Fig. 3A–D). Gain of a single gene copy was frequent (>5% of genes studied) in the RENCA and P815 lines, but amplifications of more than one extra copy much less so. We observed few deletions in the cell lines, although the most common feature across the models was the heterozygous or homozygous deletion of the *Cdkn2a* tumor suppressor gene (found in 9 of 11 cell lines; Fig. 3B).

Comparing mutational status permits model selection for tumor-targeted therapies

We also characterized the somatic mutational status of these genes using WES on a subset of the murine *in vitro* cell lines and further investigated 64 prominent cancer genes using targeted deep sequencing (Supplementary Table S3 and Supplementary Fig. S3). Our analysis revealed that several tumor cell lines did not carry mutations prevalent in the matched clinical disease. For example, Pan02 is often used as a pancreatic cancer model but lacked mutations in the *Kras* gene, which are observed in >90% of human pancreatic cancers (33) so it may only be a relevant model for a rare subtype of the disease. CT26 cells harbored mutations in the *Apc* and *Kras* genes, which are frequently observed in human colorectal cancer (34), but lacked the frequent mutation in *Trp53*. In contrast, LL/2 had many of the major mutations found in lung cancer, such as *Trp53* and a *Cdkn2a* deletion (35). The B16 lines bore a mutation in the *Braf* gene, as is frequently observed in human melanoma (36); however, this mutation was not analogous to the V600E mutation that underlies sensitivity to BRAF inhibitors (37). Comparison of the mutational profile of the murine tumor cell lines with frequently mutated genes found in the cancer type from the same tissue of origin revealed that, although the cell lines carried at least one recurrent mutation seen in the corresponding cancer type, 4 out of 9 models analyzed lacked mutations in the gene most frequently mutated in the corresponding human cancer type (Supplementary Fig. S4). The mutational status of immune-relevant genes was also evaluated across the cell lines to investigate whether cell-intrinsic genetic changes were present that could affect the ability of cell lines to recruit an immune response (Fig. 3D). We found that the most prevalent aberrations affected the complement system, including 6 of the top 50 most mutated or amplified genes in the dataset. Tumor-derived complement has been previously shown to both promote tumor growth but also contribute to the immune surveillance of tumors (reviewed in ref. 38) and even impact the tumor immune infiltrate by affecting the number of infiltrating $CD8^+$ T cells and myeloid cells, although these immunomodulatory effects are very context-dependent (39, 40). Several other genes with aberrations in the cell lines have also been shown to affect tumor growth such as fibronectin (*Fn1*; ref. 41), *Cd40* (42), or *Nfatc3* (43). This analysis also revealed that CT26 and MC38 (both derived from carcinogen-induced colorectal tumors) had

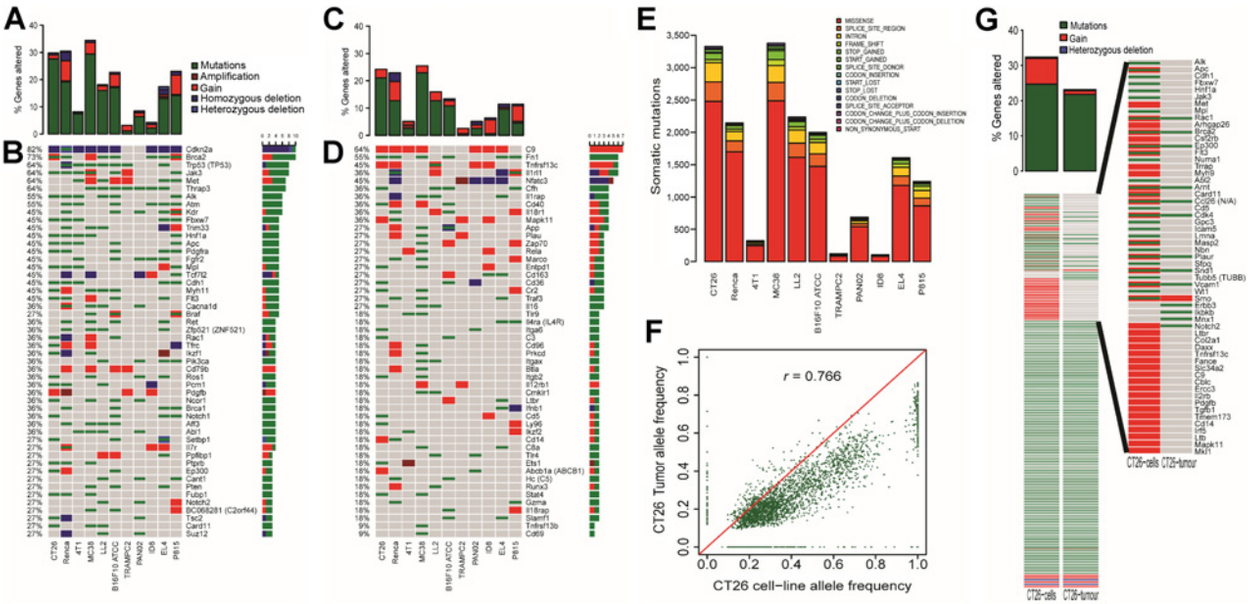

Figure 3.

Profiling of somatic mutations reveals heterogeneity across syngeneic models. Profiling by aCGH, whole-exome and targeted sequencing across 11 cell lines showing (**A**) the percentage of altered genes from 332 cancer-associated genes (selected from the COSMIC database where both copy number and mutational status data was available), (**B**) the top 50 most altered cancer-associated genes, (**C**) the percentage of altered genes from 252 immune-related genes (from the Nanostring nCounter Mouse Immunology panel gene list, excluding those already present in the cancer-associated gene list, and where both copy number and mutational status data was available), and (**D**) the top 50 most altered immune-related genes. Somatic mutations and CNVs are marked for each gene with the percentage of samples altered along the side of the heatmap. Sideway bargraphs show the total number of genomic alterations across samples, with genes ordered genes from most to least altered. Human homolog genes are stated in brackets beside the mouse gene names where these differ. **E,** Number and type of somatic mutations in protein-coding regions across cell lines. **F,** Somatic mutant allele frequency of protein-coding genes in the CT26 tumor compared with the CT26 cell line. Pearson correlation coefficient is also reported. **G,** Somatic mutations and CNVs (determined using Seq2C from WES data) of 177 cancer or immune system–associated genes in the CT26 cell line and tumor. Gene aberrations that are not found in both the cell line and tumor are in the enlarged display.

the highest somatic nonsynonymous mutational burden, with 2,955 and 3,018 mutations, respectively (Fig. 3E). ID8, derived from a spontaneous tumor, had the lowest mutational burden (102 mutations), followed by TRAMP-C2, derived from a tumor in a genetically engineered mouse (104 mutations). Thus, mutational burden appeared to be associated with the method of cell line generation in this panel, with cell lines derived from carcinogen-induced tumors having on average a higher mutational burden (1,827 mutations) than spontaneous (1,220 mutations) or GEMM-derived tumors (104 mutations).

Given that clonal selection and evolution can take place during *in vivo* tumor development, we performed WES of CT26 cells grown *in vitro* and *in vivo* (Fig. 3F and G). In the tumor, we detected 2,580 out of 2,955 (87.3%) somatic mutations found in the cell line. A high correlation ($r = 0.766$) was observed between the mutant allele frequency *in vitro* versus *in vivo* (Fig. 3F). Disparities in these data may be due to the use of an unfractionated tumor preparation for this analysis. There were genomic alterations in 57 cancer and immune-relevant genes found in the CT26 cell line which were not detected in the tumor, but these were mostly copy number gains that are more difficult to accurately quantify in heterogeneous *in vivo* samples (Fig. 3G). There were only four somatic mutations detected in the tumor which were not in the cell line (*Erbb3*, *Ikbkb*, *Mnx1*, and *Notch2*). These could have arisen due to selective pressures at play in the tumor microenvironment.

Transcriptomic comparison reveals striking immunologic heterogeneity

To investigate the baseline characteristics of the syngeneic tumor models that could underlie their differential responsiveness to immune-checkpoint blockade, we analyzed the transcriptomes of untreated established *in vivo* tumors. Pathway enrichment of differentially expressed genes in tumors revealed activation of multiple immune pathways with a high degree of heterogeneity across the models. These included innate immune–related pathways, such as pattern recognition receptors, IL8, TREM1, phagocytosis, and IL6 signaling (Fig. 4A). These pathways revealed reduced activation in tumors from B16 cell lines compared with other models. However, a limited number of pathways (PPAR, RXR, LXR, and PTEN) were more highly activated in the B16 tumors compared with the other models. These data supported the hypothesis that tumors from B16 cell lines are more immunologically "silent" compared with other tumor types, potentially underlying their reduced responsiveness to immune-checkpoint blockade. Hierarchical cluster analysis (HCA) revealed that the pathway activation profile in CT26 tumors was not substantially different from those of other tumor types, suggesting that transcriptomic differences do not completely define response to immune-checkpoint inhibitors (Fig. 4A). We also specifically investigated the expression of MHC class I and II pathway genes in the tumors and found that the B16 tumors, TC1 and LL/2 had less

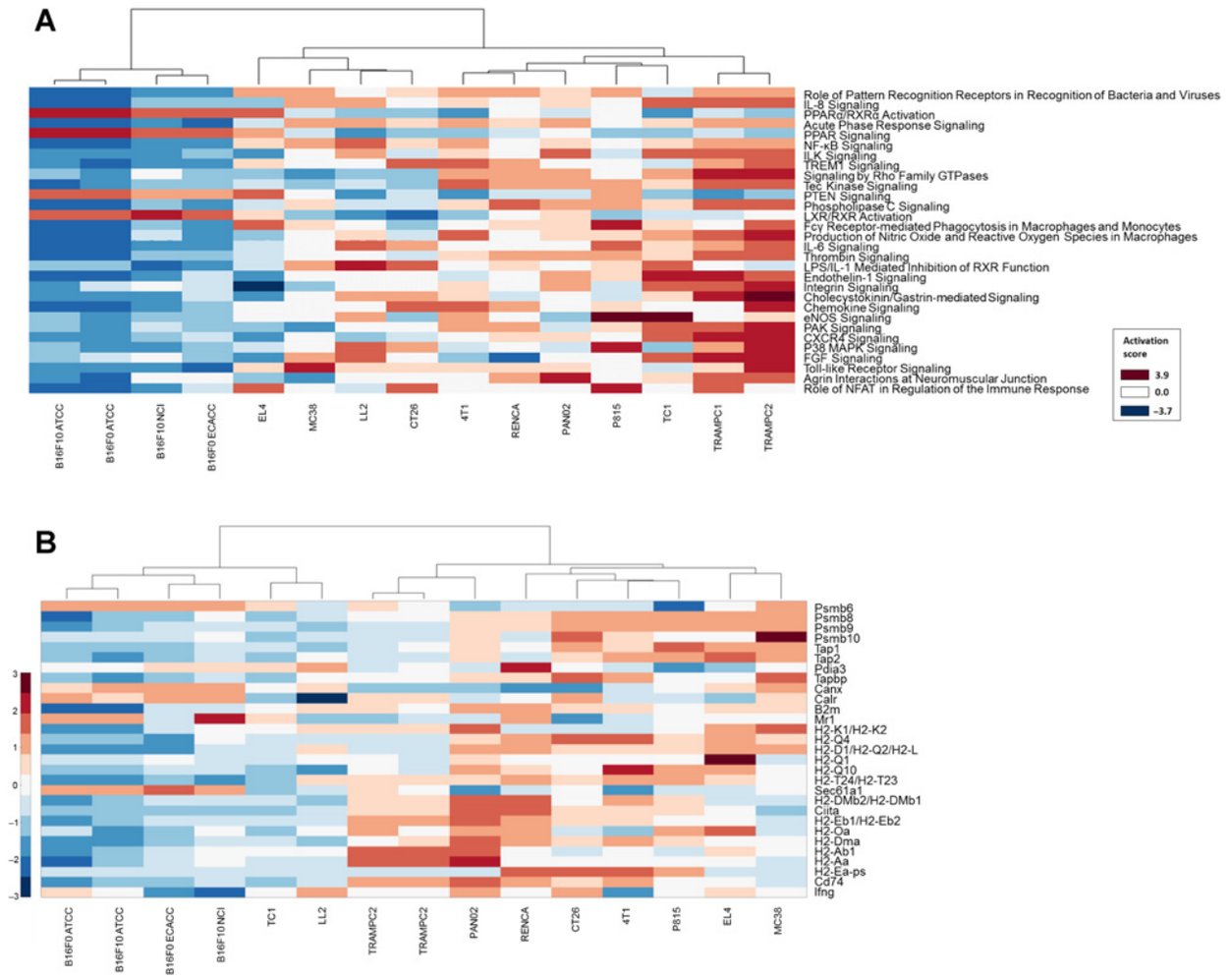

Figure 4.

Transcriptomic analysis of *in vivo* tumors reveals predominance of immune pathways among differentially expressed genes and reduced immune involvement in B16 tumors. Transcriptomic analysis of murine syngeneic *in vivo* tumor samples showing (**A**) a clustergram of differentially expressed gene-sets per model (FC $\pm$ 2.0, FDR $\leq$ 0.05) where the top ten highest and lowest pathway Z scores (IPA comparison tool) per model were selected (sorted for nondisease canonical pathways). HCA (normalized, Ward linkage and Euclidean distance) for models only, with pathways ranked by absolute activation score (summed absolute Z score across all 15 lines). **B,** Clustergram of murine syngeneic *in vivo* tumor samples based on differential expression of MHC class I and II pathway genes. HCA (normalized, Ward linkage and Euclidean distance) for models only, of normalized log2 gene expression intensity.

expression of these genes compared with the other models. The TRAMP tumors had low expression of MHC class I pathway genes, whereas the MC38 tumors had low expression of MHC class II pathway genes (Fig. 4B).

To determine whether differences in the tumor immune infiltrate could be affecting responsiveness to immune-checkpoint blockade, we investigated the expression of immune cell type–specific genes. Unsupervised HCA revealed clustering by tumor model and clear changes in expression, suggesting variation in tumor immune infiltrates across the models (Fig. 5). Several findings supported the validity of this approach, such as the elevated expression of a subset of mast cell–specific genes including *Kit* (20-fold increase compared with the SPS tumor control group), *Ctsg* (22-fold increase), and *Cma1* (2.5-fold increase), which occurred only in the P815 mastocytoma tumors where these genes are expected to be expressed in the tumor cells, as well as potentially in the immune infiltrate. B16 tumors again appeared immunologically "silent" with low expression of immune cell type–specific genes, apart from some NK-cell–specific genes. Elevated gene expression was observed for cytotoxic cell–specific genes *Gzma* (5.2-fold increase) and *Klrd1* (1.8-fold increase) in the CT26 tumors, potentially linking effector function of tumor-infiltrating immune cells and responsiveness to immune-checkpoint inhibitors.

Flow cytometric immune profiling reveals heterogeneity in tumor immune infiltrates across models

Given the diversity in the expression of immune-related genes, we further profiled the tumor immune infiltrate across both our immune-checkpoint blockade responsive and nonresponsive models by flow cytometry. Tumors were collected at an average volume of 150 mm^3, as this often corresponds to the tumor

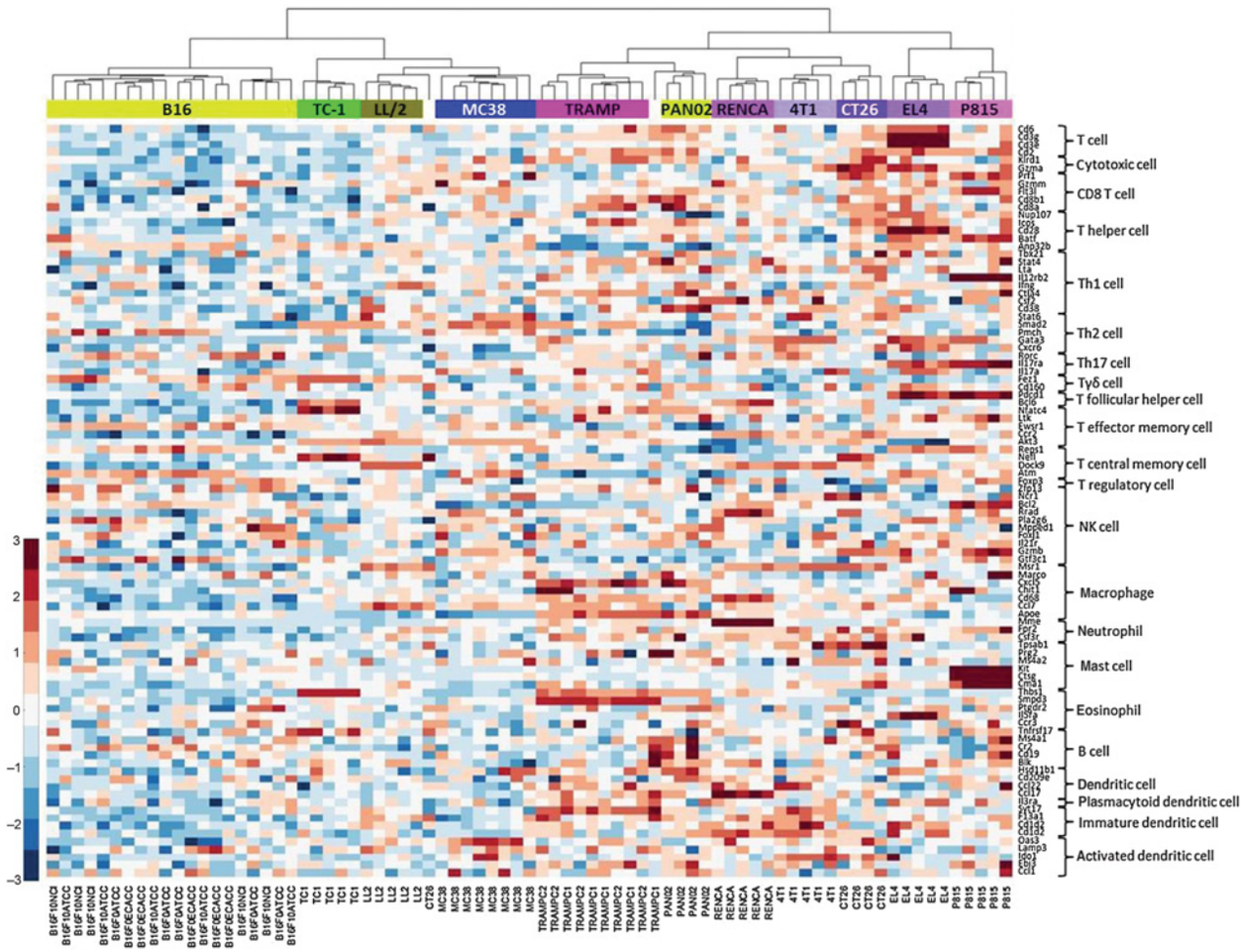

Figure 5.

Differences in immune cell type–specific gene expression suggest marked heterogeneity in the tumor immune infiltrate between models. Clustergram of murine syngeneic *in vivo* tumor samples based on differential expression of immune cell type–annotated genes from the Nanostring nCounter PanCancer Immune Profiling Panel gene-list. HCA (normalized, Ward linkage and Euclidean distance) of normalized $\log_2$ gene expression intensity with each column representing one individual mouse, $n \geq 4$ replicates per tumor model. Clustered for samples, with genes ordered by mouse cell type annotation.

volume at initiation of dosing in activity studies. The immune infiltrate was profiled by staining for 9 nonoverlapping innate and adaptive cell phenotypes and their frequency determined both as a proportion of the $CD45^+$ cells and as absolute cell count per mm^3 of tumor. Immune cell numbers per mm^3 of tumor revealed striking variations across models (Fig. 6A and B). B16F10 AP-3 tumors contained the smallest immune infiltrate with roughly 800 $CD45^+$ cells per mm^3, whereas LL/2 tumors had the largest infiltrate with 5,500 $CD45^+$ cells per mm^3 ($P < 0.0001$). Moreover, the relative proportions of immune cell types also differed profoundly. For example, 4T1 tumors predominantly contained granulocytic myeloid-derived suppressor cells (gMDSCs, >40% of their immune infiltrate), whereas LL/2 and MC38 tumors contained mainly monocytic MDSCs (mMDSCs, 33% and 47%, respectively). Notably, CT26 tumors contained the highest number of NK cells (520 per mm^3) and an increased proportion of granzyme B^+ NK cells compared with other models (Fig. 6C). In addition, the CT26 and RENCA models contained the highest proportions of T cells. Within the $CD8^+$ T-cell population, the proportion of reinvigorated cells [expressing markers of T-cell exhaustion (PD-1 and Eomes) but having undergone a reversal of this exhaustion leading to upregulation of Ki67 and granzyme B; ref. 44)] was highest in CT26 tumors (Fig. 6D). The absolute cell counts revealed that CT26, and to a lesser extent RENCA, tumor immune infiltrates were rich in cytotoxic immune cells whereas 4T1, B16F10 AP-3, LL/2, and MC38 are predominantly composed of cell types considered to be immunosuppressive.

In tumor lysates, the highest expression of several proinflammatory cytokines such as IL2, IFNγ, TNFα, and IL1β were found in the CT26, MC38, and RENCA models (Fig. 6E). In contrast, higher levels of Th2-associated cytokines such as IL4 and IL10 were found in the MC38, 4T1, and B16F10 AP-3 models. Notably, KC/GRO, a chemoattractant for neutrophils and MDSCs, was elevated in the MDSC-rich 4T1, MC38, and LL/2 tumors.

To expand our observations, we also assessed spleens and tumor-draining lymph nodes from these animals (tissues from non-tumor–bearing mice were included to highlight changes from baseline). An >8-fold increase in splenic gMDSCs/

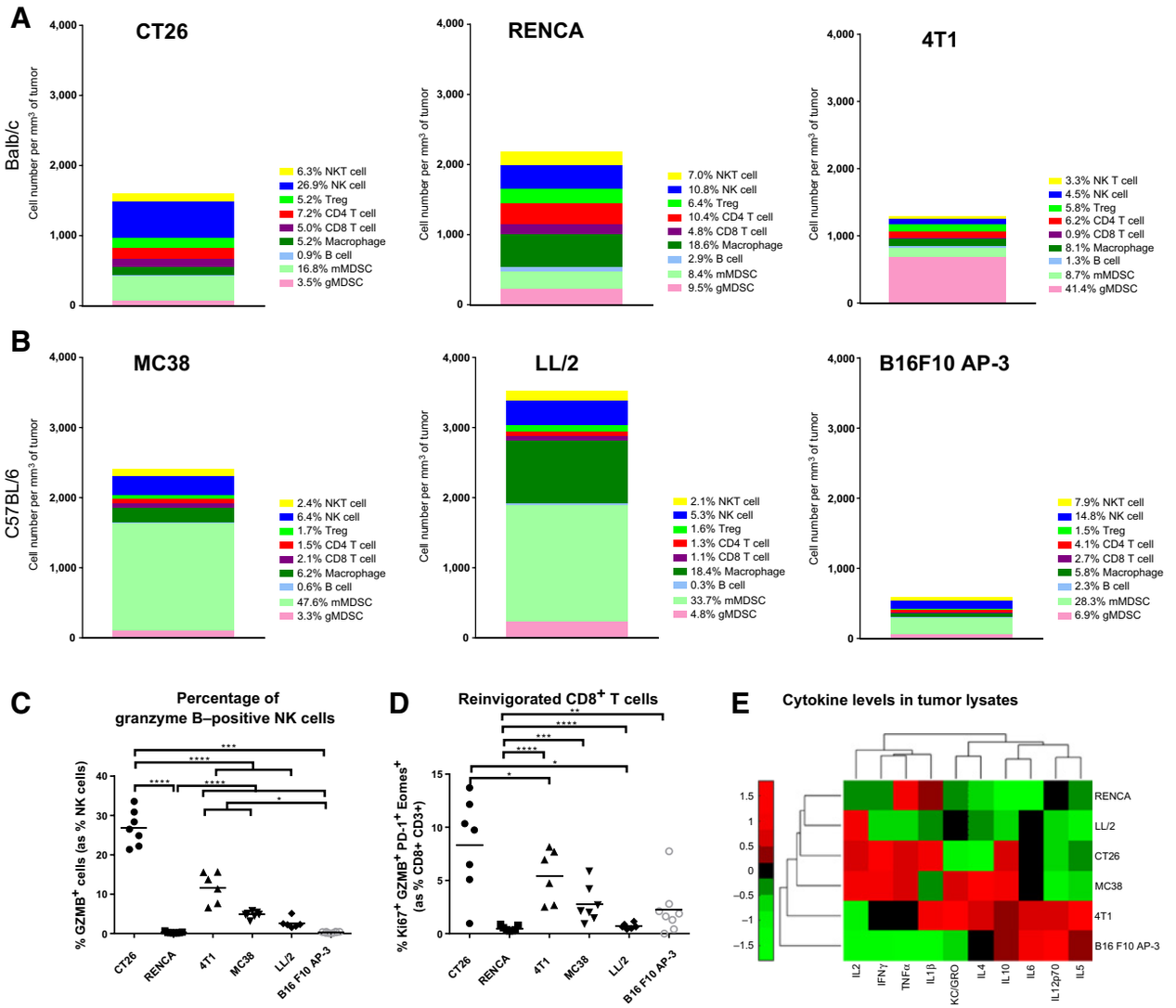

Figure 6.

Immune phenotyping reveals profound differences in the tumor microenvironment across different syngeneic models. Flow cytometric analysis of the tumor immune cell infiltrate in (**A**) 3 BALB/c models (CT26, RENCA and 4T1) and in (**B**) 3 C57BL/6 models (MC38, LL/2, and B16F10 AP-3) showing cell counts per mm^3 of tumor for 9 immune cell types and their frequencies (as percentages of $CD45^+$ cells). $n \geq 6$ mice per group. **C,** Percentages of NK cells that were positive for granzyme B in each model. **D,** Percentages of $CD8^+$ T cells expressing Eomes, PD-1, Ki67, and granzyme B in each model. *, $P < 0.05$; **, $P < 0.01$; ***, $P < 0.001$; ****, $P < 0.0001$, Tukey multiple comparisons test. **E,** Heatmap of the logged values for expression of 10 cytokines in the lysates of 6 tumors. Data are representative of trends observed in at least two independent experiments.

neutrophils was observed in 4T1 tumor-bearing mice compared with tumor-naïve mice ($P = 0.0028$; Fig. 7A), mirroring the predominance of these cells in the tumor (Fig. 7E). A common finding was that spleens from tumor-bearing mice had smaller percentages of T cells (30%) relative to tumor-naïve controls (42%; $P < 0.0001$; Fig. 7A and B). In tumor-naïve animals, a comparison of both genetic strains showed that BALB/c LNs had a larger proportion of $CD4^+$ T cells compared with C57BL/6 LNs (49.7% vs. 32.3% $P < 0.0001$), which had more B cells (13.9% vs. 23.6% $P = 0.0003$; Fig. 7C and D). In TDLNs, an expansion of B cells was seen versus control tumor-naïve LNs ($P = 0.0003$) and this was most marked in the LL/2 and MC38 models, where it was accompanied by a corresponding decrease in the proportions of T cells and NK cells. Despite the striking contrasts in the composition of the tumor immune infiltrate (Fig. 7E and F), this was not mirrored in the TDLNs.

Discussion

Murine syngeneic tumor models play a central role in the advancement of novel immunotherapies; however, there is a need to fully elucidate their distinct molecular and immunologic characteristics. In the current study, we provide a resource to rationalize the selection of syngeneic models to test specific hypotheses; increasing the value of such studies and reducing the numbers of animals used in scientific research. In addition to

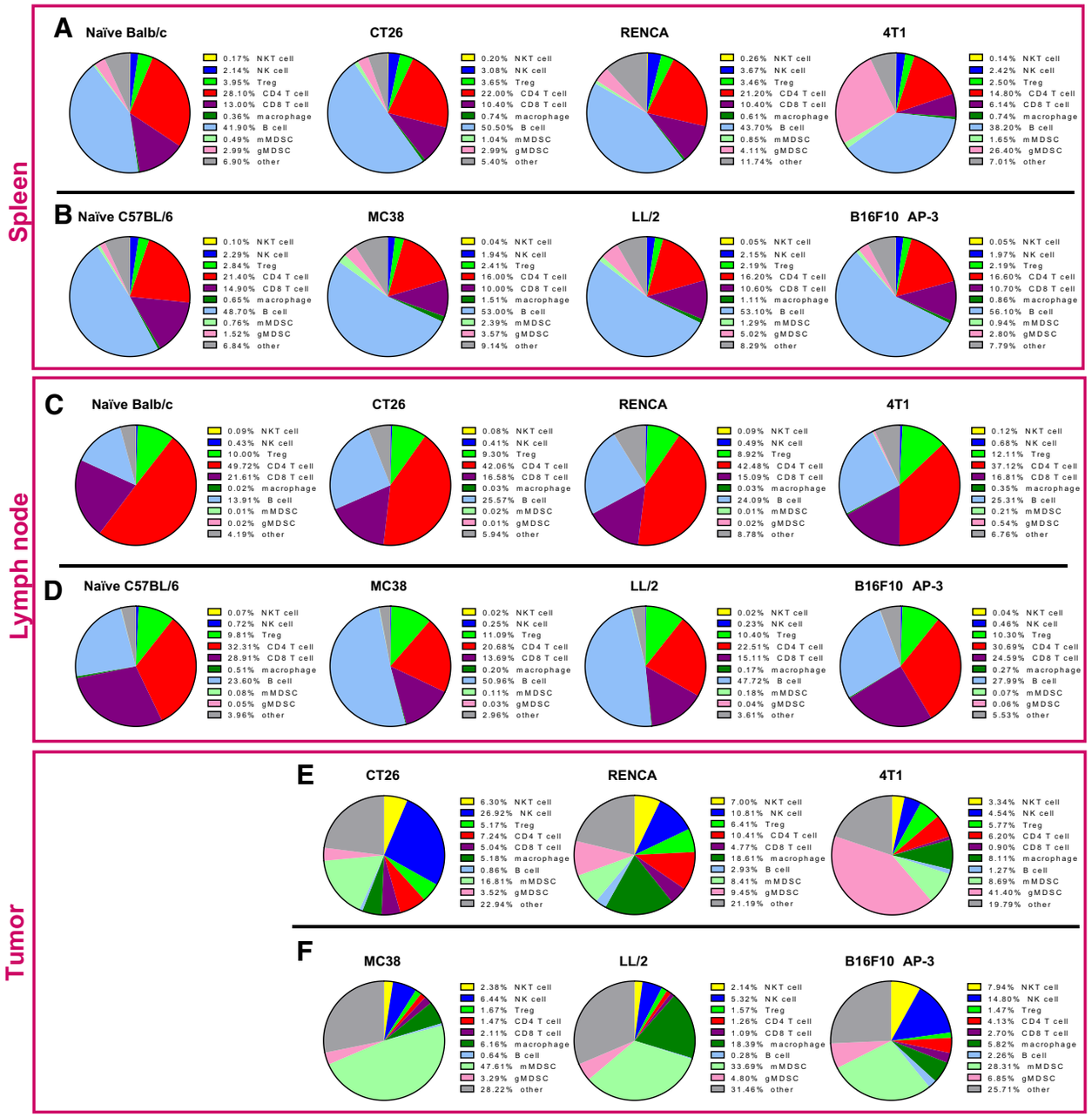

Figure 7.

Frequencies of immune cell types show much stronger variations between tumor types in the tumor infiltrate compared with the spleen and tumor-draining lymph nodes. Flow cytometric analysis of the immune cell composition of (**A** and **B**) the spleen, (**C** and **D**) the tumor-draining lymph node (or inguinal lymph nodes in naïve mice) and (**E** and **F**) the tumor of mice bearing (**A, C** and **E**) 3 BALB/c models (CT26, RENCA and 4T1) or control naïve Balb/c mice and of mice bearing (**B, D** and **F**) 3 C57BL/6 models (MC38, LL/2, and B16F10 AP-3) or control naïve C57BL/6 mice, showing frequencies of 9 immune cell types (as percentages of $CD45^+$ cells). $n \geq 6$ mice per group. Data is representative of trends observed in at least 2 independent experiments.

characterizing the tumor microenvironment, we provide a molecular annotation of these models to describe the specific driver mutations that can be leveraged to guide immunotherapy combinations with molecularly targeted therapies. Indeed, such combinations hold considerable promise to broaden the patient population benefiting from immunotherapy.

We have identified models in which the dominant immunologic phenotype of the tumor is associated with myeloid immunosuppression, for example, increased gMDSC and mMDSC infiltration in the 4T1, MC38, and LL/2 models. We have also identified models, particularly the B16F10 AP-3, that are poorly infiltrated by immune cells. In contrast, other models are both rich

in tumor immune cell infiltration but also harbor more balanced populations of effector and suppressive immune cell populations, for example, CT26 and RENCA. This immunologic diversity broadly recapitulates the diversity of tumors observed clinically and therefore provides a powerful resource to evaluate different immunotherapies in the context of these distinct microenvironments. An example of this could be the selection of an immunologically "cold" tumor model such as B16F10-AP3 to evaluate the capacity of treatment to transform the tumor microenvironment leading to enhanced immune priming and immune cell infiltration into tumors, for example, with radiotherapy, agonism of pattern-recognition receptors, or through vaccine approaches. Likewise, modeling of immunologically "hot" tumors is also translationally relevant and the CT26 or RENCA models may provide suitable settings to evaluate experimental therapeutics.

Our analysis of the somatic mutation profile of the murine cell lines reveals genetic disparities when compared with the prevalent mutations in the analogous clinical disease. Examples of these include *Trp53* in CT26 or *Kras* in Pan02. However, many of the genes that are commonly mutated in the clinical setting are also mutated across the preclinical models tested, offering opportunities to understand the impact of these mutations in a syngeneic setting. In particular these data will enable researchers to identify models with both the relevant pathway addiction for a defined molecular target, for example, MEK, BRAF (45), and overlay this with a characterized microenvironment to permit pertinent and appropriate combinations of immunotherapy and small-molecule inhibitors to be evaluated.

Our study also highlights differences between the activity of immunotherapies in a preclinical setting and clinical activity in the analogous human cancer type. An example of this is the contrast between the strong preclinical responses to anti–CTLA-4 and anti–PD-L1 treatment in the CT26 model, derived from a murine colorectal tumor, and clinical responses in colorectal cancer in which, with the exception of patients with mismatch repair–deficient disease, limited activity with immune-checkpoint blockade has been observed to date (46). Poor responses to treatment with either anti–PD-L1 or anti–CTLA-4 were observed in the B16 model, derived from a murine melanoma, which contrasts with the encouraging responses reported for melanoma in the clinic (47). However, when these responses are assessed in the context of the distinct tumor microenvironments observed across the preclinical models, our results are broadly in agreement with clinical findings, which demonstrate an association between $CD8^+$ T-cell infiltration into the tumor and outcome following immune-checkpoint blockade (9, 48, 49). Indeed, our work also revealed that tumors such as CT26, in which the immune infiltrate contains greater numbers of cytotoxic immune cells such as $CD8^+$ T cells and NK cells, were more responsive to immune-checkpoint blockade than those with comparatively little immune or predominantly immunosuppressive infiltrate. Thus, we conclude that the power of the models lies in recapitulating both a distinct phenotype of tumor microenvironment and mutation profile, rather than directly relating to the analogous human disease setting.

An interesting observation was that although the composition of the tumor microenvironment across the syngeneic models tested was strikingly varied, this contrasted starkly with the relative homogeneity in the immune phenotype observed in secondary lymphoid organs such as the tumor-draining lymph nodes and spleens. This homogeneity was also reflected by gene expression, with markedly fewer differentially expressed gene pathways observed in these tissues when compared with those in the tumors (Supplementary Fig. S5). Overall, these data suggest that the greatest differences between models may result from the preferential chemoattraction, retention, and or differentiation of immune cells within the tumor microenvironment rather than from skewing of the systemic immune response, and therefore the likely factors that are driving response reside within the tumor rather than within the peripheral immune compartments. Again, this finding is also in keeping with the majority of data from the clinic to-date, where the most promising predictive biomarkers have been found in tumor tissue, rather than in peripheral blood (49).

Several of our findings are concordant with previous observations, such as the predominant loss of *Cdkn2a* among the cell lines, which has been described to result from cell culture–selective pressures (50) and is also prevalent across multiple human cancer types (51). Previous studies have also shown that different syngeneic tumor models can respond differently to treatment (16, 49, 52). It has been hypothesized that these differences could be due to variability in immunogenicity of the models (13) but, until now, the similarities and differences between these models have not been comprehensively characterized. The most extensive study, to our knowledge, included 6 commonly used syngeneic models with analysis limited to the expression of 27 immune-related genes and staining for 4–6 immune cell types by IHC and flow cytometry (52). We also saw a high level of agreement in somatic mutation results with previous genetic characterization of the CT26 cell line, with >60% of mutated genes matching those in the study by Castle and colleagues (53, 54). Although another study described fewer somatic mutations in CT26 and 4T1, 80%–90% of those mutated genes matched our results (54) and the relative proportions of somatic mutations was conserved, with >10-fold more mutations in CT26 compared with the 4T1. Likewise, comparison of our somatic mutation results in the ATCC B16F10 line with those in Castle and colleagues (55) showed over 90% concordance in the mutated genes found in both studies including *Brca2*, *Trp53*, *Jak3*, *Atm*, *Pten*, and *Mdm1*. Disparities in somatic mutations between studies could be due to differences in cut-off levels, sensitivity and methodology, as well as cell line divergence. Our profiling of CNV, using both aCGH and WES analysis paired with the BALB/c mouse background, did not show the same large regions of triploidy and tetraploidy in CT26 seen by Castle and colleagues (53). However, for such multichromosomal regions, it is unlikely that this would be due to divergence in the CT26 cell lines, but rather due to methodological differences such as stringency of CNV calling.

In conclusion, we provide extensive characterization of a range of commonly used murine syngeneic models to rationalize model selection based on the biology of the tumor cell and the tumor microenvironment. Moreover, a greater understanding of model biology allows more robust alignment between response, mechanism of action, and the biology of human cancer subtypes that may ultimately improve the efficiency of drug discovery.

Disclosure of Potential Conflicts of Interest

P. Brohawn is an employee of AstraZeneca. R. Stewart has ownership interest (including patents) in AstraZeneca. No potential conflicts of interest were disclosed by the other authors.

Authors' Contributions

Conception and design: S.I.S. Mosely, R.C.A. Sainson, R. Leyland, J. Coates Ulrichsen, P. Brohawn, M. McCourt, J.A. Harper, M. Morrow, V. Valge-Archer, R. Stewart, R.W. Wilkinson

Development of methodology: S.I.S. Mosely, R.C.A. Sainson, R. Leyland, A. Watkins, M. McCourt, J.A. Harper, M. Morrow, R. Stewart, S.J. Dovedi

Acquisition of data (provided animals, acquired and managed patients, provided facilities, etc.): S.I.S. Mosely, D.M. Greenawalt, S. Mullins, L. Pacelli, D. Marcus, J. Anderton, A. Watkins, J. Coates Ulrichsen, P. Brohawn, J.A. Harper, R.W. Wilkinson

Analysis and interpretation of data (e.g., statistical analysis, biostatistics, computational analysis): S.I.S. Mosely, R.C.A. Sainson, J.-O. Koopmann, D.M. Greenawalt, M.J. Ahdesmaki, R. Leyland, D. Marcus, A. Watkins, P. Brohawn, B.W. Higgs, V. Valge-Archer, S.J. Dovedi, R.W. Wilkinson

Writing, review, and/or revision of the manuscript: S.I.S. Mosely, R.C.A. Sainson, J.-O. Koopmann, D.M. Greenawalt, A. Watkins, P. Brohawn, B.W. Higgs, J.A. Harper, M. Morrow, V. Valge-Archer, R. Stewart, S.J. Dovedi, R.W. Wilkinson

Administrative, technical, or material support (i.e., reporting or organizing data, constructing databases): R. Leyland, J. Anderton, S.J. Dovedi

Study supervision: R.C.A. Sainson, J. Coates Ulrichsen, M. McCourt, M. Morrow

Acknowledgments

Thanks to Athula Herath, Robert Kozarski, and Wen Wu for advice on experimental design and statistical analysis, to Tristan Lubinski for data analysis and to the biological services unit and core tissue culture facility at MedImmune for technical support. We also acknowledge the assistance provided by the Oncology Research team, in particular Olivia Harris, Marianna Papaspyridonos, and Amy Popple, for their input into the development of flow cytometric analysis of mouse tumor models.

Grant Support

All studies were funded by MedImmune and AstraZeneca.

The costs of publication of this article were defrayed in part by the payment of page charges. This article must therefore be hereby marked *advertisement* in accordance with 18 U.S.C. Section 1734 solely to indicate this fact.

Received May 20, 2016; revised October 24, 2016; accepted November 11, 2016; published OnlineFirst December 6, 2016.

References

1. Maio M, Grob JJ, Aamdal S, Bondarenko I, Robert C, Thomas L, et al. Five-year survival rates for treatment-naive patients with advanced melanoma who received ipilimumab plus dacarbazine in a phase III trial. J Clin Oncol 2015;33:1191–6.
2. Brahmer J, Reckamp KL, Baas P, Crino L, Eberhardt WE, Poddubskaya E, et al. Nivolumab versus docetaxel in advanced squamous-cell non-small-cell lung cancer. N Engl J Med 2015;373:123–35.
3. Herbst RS, Baas P, Kim DW, Felip E, Perez-Gracia JL, Han JY, et al. Pembrolizumab versus docetaxel for previously treated, PD-L1-positive, advanced non-small-cell lung cancer (KEYNOTE-010): a randomised controlled trial. Lancet 2016;387:1540–50.
4. Smyth MJ, Ngiow SF, Ribas A, Teng MW. Combination cancer immunotherapies tailored to the tumour microenvironment. Nat Rev Clin Oncol 2016;13:143–58.
5. Topalian SL, Drake CG, Pardoll DM. Immune checkpoint blockade: a common denominator approach to cancer therapy. Cancer Cell 2015; 27:450–61.
6. Gajewski TF, Schreiber H, Fu YX. Innate and adaptive immune cells in the tumor microenvironment. Nat Immunol 2013;14:1014–22.
7. Sharma P, Allison JP. The future of immune checkpoint therapy. Science 2015;348:56–61.
8. Galon J, Costes A, Sanchez-Cabo F, Kirilovsky A, Mlecnik B, Lagorce-Pages C, et al. Type, density, and location of immune cells within human colorectal tumors predict clinical outcome. Science 2006; 313:1960–4.
9. Tumeh PC, Harview CL, Yearley JH, Shintaku IP, Taylor EJ, Robert L, et al. PD-1 blockade induces responses by inhibiting adaptive immune resistance. Nature 2014;515:568–71.
10. Snyder A, Makarov V, Merghoub T, Yuan J, Zaretsky JM, Desrichard A, et al. Genetic basis for clinical response to CTLA-4 blockade in melanoma. N Engl J Med 2014;371:2189–99.
11. Schumacher TN, Schreiber RD. Neoantigens in cancer immunotherapy. Science 2015;348:69–74.
12. McGranahan N, Furness AJ, Rosenthal R, Ramskov S, Lyngaa R, Saini SK, et al. Clonal neoantigens elicit T cell immunoreactivity and sensitivity to immune checkpoint blockade. Science 2016;351:1463–9.
13. Dranoff G. Experimental mouse tumour models: what can be learnt about human cancer immunology? Nat Rev Immunol 2012;12:61–6.
14. Gould SE, Junttila MR, de Sauvage FJ. Translational value of mouse models in oncology drug development. Nat Med 2015;21:431–9.
15. Westcott PM, Halliwill KD, To MD, Rashid M, Rust AG, Keane TM, et al. The mutational landscapes of genetic and chemical models of Kras-driven lung cancer. Nature 2014;517:489–92.
16. Grosso JF, Jure-Kunkel MN. CTLA-4 blockade in tumor models: an overview of preclinical and translational research. Cancer Immun 2013;13:5.
17. Leach DR, Krummel MF, Allison JP. Enhancement of antitumor immunity by CTLA-4 blockade. Science 1996;271:1734–6.
18. Quezada SA, Peggs KS, Curran MA, Allison JP. CTLA4 blockade and GM-CSF combination immunotherapy alters the intratumor balance of effector and regulatory T cells. J Clin Invest 2006;116:1935–45.
19. Liakou CI, Kamat A, Tang DN, Chen H, Sun J, Troncoso P, et al. CTLA-4 blockade increases IFNgamma-producing CD4+ICOShi cells to shift the ratio of effector to regulatory T cells in cancer patients. Proc Natl Acad Sci USA 2008;105:14987–92.
20. Workman P, Aboagye EO, Balkwill F, Balmain A, Bruder G, Chaplin DJ, et al. Guidelines for the welfare and use of animals in cancer research. Br J Cancer 2010;102:1555–77.
21. Zhao H, Sun Z, Wang J, Huang H, Kocher JP, Wang L. CrossMap: a versatile tool for coordinate conversion between genome assemblies. Bioinformatics 2014;30:1006–7.
22. Li H, Durbin R. Fast and accurate short read alignment with Burrows-Wheeler transform. Bioinformatics 2009;25:1754–60.
23. Garrison E, Marth G. Haplotype-based variant detection from short-read sequencing. arXiv: Cornell University Library; 2012. Available from: https://arxiv.org/abs/1207.3907.
24. Lai Z, Markovets A, Ahdesmaki M, Chapman B, Hofmann O, McEwen R, et al. VarDict: a novel and versatile variant caller for next-generation sequencing in cancer research. Nucleic Acids Res 2016;44:e108.
25. Talevich E, Shain AH, Botton T, Bastian BC. CNVkit: Genome-Wide Copy Number Detection and Visualization from Targeted DNA Sequencing. PLoS Comput Biol 2016;12:e1004873.
26. Forbes SA, Beare D, Gunasekaran P, Leung K, Bindal N, Boutselakis H, et al. COSMIC: exploring the world's knowledge of somatic mutations in human cancer. Nucleic Acids Res 2015;43:D805–11.
27. Langmead B, Salzberg SL. Fast gapped-read alignment with Bowtie 2. Nat Methods 2012;9:357–9.
28. Koboldt DC, Zhang Q, Larson DE, Shen D, McLellan MD, Lin L, et al. VarScan 2: somatic mutation and copy number alteration discovery in cancer by exome sequencing. Genome Res 2012;22:568–76.
29. Wang K, Li M, Hakonarson H. ANNOVAR: functional annotation of genetic variants from high-throughput sequencing data. Nucleic Acids Res 2010;38:e164.
30. Demidenko E. Statistical comparison of color cancer cell images. Oncol Rep 2006;15:1077–9.
31. Heitjan DF. Biology, models, and the analysis of tumor xenograft experiments. Clin Cancer Res 2011;17:949–51.
32. Stewart R, Morrow M, Hammond SA, Mulgrew K, Marcus D, Poon E, et al. Identification and characterization of MEDI4736, an antagonistic anti-PD-L1 monoclonal antibody. Cancer Immunol Res 2015;3:1052–62.
33. Almoguera C, Shibata D, Forrester K, Martin J, Arnheim N, Perucho M. Most human carcinomas of the exocrine pancreas contain mutant c-K-ras genes. Cell 1988;53:549–54.
34. The Cancer Genome Atlas. Comprehensive molecular characterization of human colon and rectal cancer. Nature 2012;487:330–7.

35. The Cancer Genome Atlas. Comprehensive molecular profiling of lung adenocarcinoma. Nature 2014;511:543–50.
36. Akbani R, Akdemir KC, Aksoy BA, Albert M, Ally A, Amin SB, et al. Genomic classification of cutaneous melanoma. Cell 2015;161: 1681–96.
37. Tsao H, Chin L, Garraway LA, Fisher DE. Melanoma: from mutations to medicine. Genes Dev 2012;26:1131–55.
38. Markiewski MM, Lambris JD. Is complement good or bad for cancer patients? A new perspective on an old dilemma. Trends Immunol 2009;30:286–92.
39. Cho MS, Vasquez HG, Rupaimoole R, Pradeep S, Wu S, Zand B, et al. Autocrine effects of tumor-derived complement. Cell Rep 2014;6: 1085–95.
40. Vadrevu SK, Chintala NK, Sharma SK, Sharma P, Cleveland C, Riediger L, et al. Complement c5a receptor facilitates cancer metastasis by altering T-cell responses in the metastatic niche. Cancer Res 2014; 74:3454–65.
41. Sengupta S, Nandi S, Hindi ES, Wainwright DA, Han Y, Lesniak MS. Short Hairpin RNA-mediated fibronectin knockdown delays tumor growth in a mouse glioma model. Neoplasia 2010;12:837–47.
42. Kim H, Kim Y, Bae S, Kong JM, Choi J, Jang M, et al. Direct Interaction of CD40 on tumor cells with CD40L on T cells increases the proliferation of tumor cells by enhancing TGF-beta production and Th17 differentiation. PLoS One 2015;10:e0125742.
43. Shou J, Jing J, Xie J, You L, Jing Z, Yao J, et al. Nuclear factor of activated T cells in cancer development and treatment. Cancer Lett 2015;361: 174–84.
44. Twyman-Saint\sVictor C, Rech AJ, Maity A, Rengan R, Pauken KE, Stelekati E, et al. Radiation and dual checkpoint blockade activate non-redundant immune mechanisms in cancer. Nature 2015;520:373–7.
45. Liu L, Mayes PA, Eastman S, Shi H, Yadavilli S, Zhang T, et al. The BRAF and MEK inhibitors dabrafenib and trametinib: effects on immune function and in combination with immunomodulatory antibodies targeting PD-1, PD-L1, and CTLA-4. Clin Cancer Res 2015;21: 1639–51.
46. Le DT, Uram JN, Wang H, Bartlett BR, Kemberling H, Eyring AD, et al. PD-1 blockade in tumors with mismatch-repair deficiency. N Engl J Med 2015;372:2509–20.
47. Ott PA, Hodi FS, Robert C. CTLA-4 and PD-1/PD-L1 blockade: new immunotherapeutic modalities with durable clinical benefit in melanoma patients. Clin Cancer Res 2013;19:5300–9.
48. Ji RR, Chasalow SD, Wang L, Hamid O, Schmidt H, Cogswell J, et al. An immune-active tumor microenvironment favors clinical response to ipilimumab. Cancer Immunol Immunother 2012;61:1019–31.
49. Herbst RS, Soria JC, Kowanetz M, Fine GD, Hamid O, Gordon MS, et al. Predictive correlates of response to the anti-PD-L1 antibody MPDL3280A in cancer patients. Nature 2014;515:563–7.
50. Hartmann C, Kluwe L, Lucke M, Westphal M. The rate of homozygous CDKN2A/p16 deletions in glioma cell lines and in primary tumors. Int J Oncol 1999;15:975–82.
51. Ruas M, Peters G. The p16INK4a/CDKN2A tumor suppressor and its relatives. Biochim Biophys Acta 1998;1378:F115–77.
52. Lechner MG, Karimi SS, Barry-Holson K, Angell TE, Murphy KA, Church CH, et al. Immunogenicity of murine solid tumor models as a defining feature of in vivo behavior and response to immunotherapy. J Immunother 2013;36:477–89.
53. Castle JC, Loewer M, Boegel S, de Graaf J, Bender C, Tadmor AD, et al. Immunomic, genomic and transcriptomic characterization of CT26 colorectal carcinoma. BMC Genomics 2014;15:190.
54. Kim K, Skora AD, Li Z, Liu Q, Tam AJ, Blosser RL, et al. Eradication of metastatic mouse cancers resistant to immune checkpoint blockade by suppression of myeloid-derived cells. Proc Natl Acad Sci USA 2014; 111:11774–9.
55. Castle JC, Kreiter S, Diekmann J, Lower M, van de Roemer N, de Graaf J, et al. Exploiting the mutanome for tumor vaccination. Cancer Res 2012;72:1081–91.